ARTICLE   **Open Access**

Water-induced MAPbBr₃@PbBr(OH) with enhanced luminescence and stability

Kai-Kai Liu[1], Qian Liu[1], Dong-Wen Yang[1], Ya-Chuan Liang[1], Lai-Zhi Sui[2], Jian-Yong Wei[1], Guo-Wei Xue[1], Wen-Bo Zhao[1], Xue-Ying Wu[1], Lin Dong [1] and Chong-Xin Shan[1]

Abstract

Poor stability has long been one of the key issues that hinder the practical applications of lead-based halide perovskites. In this paper, the photoluminescence (PL) quantum yield (QY) of bromide-based perovskites can be increased from 2.5% to 71.54% by introducing water, and the PL QY of a sample in aqueous solution decreases minimally over 1 year. The enhanced stability and PL QY can be attributed to the water-induced methylamino lead bromide perovskite (MAPbBr₃)@PbBr(OH). We note that this strategy is universal to MAPbBr₃, formamidine lead bromide perovskite (FAPbBr₃), inorganic lead bromide perovskite (CsPbBr₃), etc. Light-emitting devices (LEDs) are fabricated by using the as-prepared perovskite as phosphors on a 365 nm UV chip. The luminance intensity of the LED is 9549 cd/m² when the driven current is 200 mA, and blemishes on the surface of glass are clearly observed under the illumination of the LEDs. This work provides a new strategy for highly stable and efficient perovskites.

Introduction

In recent years, lead halide perovskites (LHPs) APbX₃ (A = CH₃NH₃⁺/CH(NH₂)₂⁺/Cs⁺, X = Cl⁻/Br⁻/I⁻) have emerged as promising materials for photovoltaics and light-emitting diodes due to their attractive optical and electrical properties, such as high photoluminescence (PL) quantum yield (QY), narrow emission spectrum, tuneable emission wavelength, high absorption coefficient, and long carrier diffusion length[1–11]. Profound developments have been witnessed in the fields of solar cells[12–15], solid-state light-emitting diodes[11,16–20], photodetectors[21–23], and lasers[7,24,25]. However, the poor stability of LHPs, especially in water and polar solvents, remains a crucial issue that hampers their applications.

The origin of the instability of LHPs is generally attributed to their low formation energy, which makes these materials vulnerable to light, heat, oxygen, and moisture, especially when water is involved[26–29]. In addition, the ions of LHPs with discrete components are exchanged with each other quickly, which results in severe shifts in the emissions. Strategies for improving the stability of LHPs can be classified into three types: compositional engineering, surface engineering, and matrix encapsulation[30]. The all-inorganic lead perovskite (CsPbBr₃), where methylamino (MA) ions are replaced with Cs ions, shows much higher stability, including thermal and environmental stability, than organic–inorganic perovskite[31]. Although the thermal and environmental stability of this perovskite has been improved through compositional engineering, poor moisture stability is still a serious problem. The stability of LHPs improves greatly when they are covered with long-chain surface agents, which has been widely demonstrated by researchers. However, LHPs usually lose surface ligands and then reunite and lose their colloidal stability during purification[32]. Matrix encapsulation has been applied to effectively enhance the stability and PL efficacy of perovskite. For example, Jia et al. prepared CsPbX₃/Cs₄PbX₆ core/shell perovskite

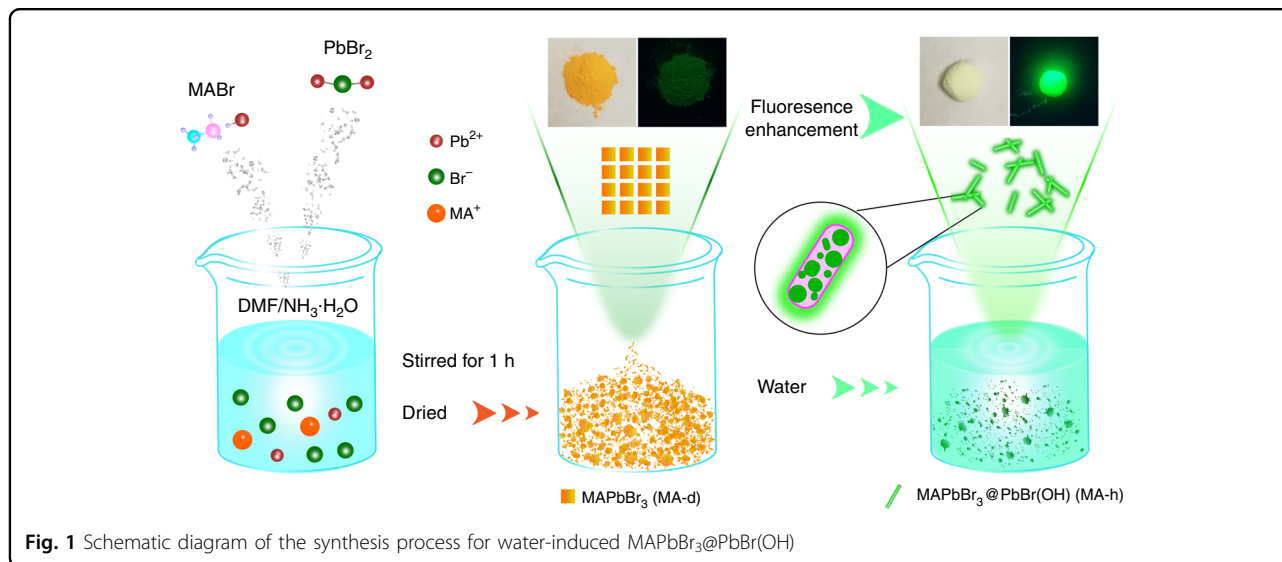Correspondence: Lin Dong (ldong@zzu.edu.cn) or Chong-Xin Shan (cxshan@zzu.edu.cn)
¹Henan Key Laboratory of Diamond Optoelectronic Materials and Devices, Key Laboratory of Material Physics, Ministry of Education, School of Physics and Microelectronics, Zhengzhou University, Zhengzhou 450052, China
²State Key Laboratory of Molecular Reaction Dynamics, Dalian Institute of Chemical Physics, Chinese Academy of Sciences, 457 Zhongshan Road, Dalian 116023, China

Fig. 1 Schematic diagram of the synthesis process for water-induced MAPbBr$_3$@PbBr(OH)

nanocrystals by applying a seeded growth approach, which provided improved PL QY. Wang et al. produced a Rb$_4$PbBr$_6$ shell to protect CsPbX$_3$ through the rubidium oleate posttreatment method. Similarly, Tang et al. reported a kind of CsPbBr$_3$/CdS core/shell structure using a hot-injection method. Embedding CsPbBr$_3$ into SiO$_2$ or the pores of mesoporous silica can also improve the stability of the perovskite[33–37]. Although most inorganic matrices are dense and thermally stable, it is difficult to controllably form an inorganic protective layer covering perovskite quantum dots (QDs) due to the high synthetic temperature and relatively complicated synthesis conditions. Furthermore, the introduction of expensive or toxic elements further hinders the applications of perovskites. Moreover, the phase separation between LHPs and protection media still remains, resulting in size variation, low loading, broad spectra, and low PL QY. Some researchers have demonstrated the positive role of water in the synthesis of LHPs[38–40]. For example, Andrey et al. synthesized stable CsPbBr$_3$ nanocrystals by introducing a suitable amount of water into the reaction mixture[41]. It is important to note that when a large amount of water was introduced in this system, the perovskite still decomposed. Atanu and Kwang demonstrated the aqueous synthesis of various hybrids and all-inorganic halide perovskites in acidic and basic media[42]. The perovskites were stable in water for more than 6 months, but the PL QY of the as-prepared methylamino lead bromide perovskites (MAPbBr$_3$) was only 11.7%. These observations indicate that there exists a solubility equilibrium between the crystallization of perovskite and its saturated ionic components in water. Thus, the luminescence and stability of LHPs may be enhanced by water by choosing appropriate pH, metal halide salts, and different organic components.

In this work, we show that the PL QY and stability of LHPs can be greatly enhanced by adding water, and the PL QY of the LHPs can be increased from 2.50% to 71.54%, while that of a sample in aqueous solution decreases minimally after 1 year. This strategy is universal to MAPbBr$_3$, formamidine lead bromide perovskites (FAPbBr$_3$), and CsPbBr$_3$. UV-pumped LEDs have been fabricated by using the prepared perovskites as phosphors, and blemishes including scratches, dust, and fingerprints on the surface of glass can be observed clearly under the illumination of the LEDs, indicating that the LEDs are suitable for manual defect detection.

Results

Structural and morphology characterization

The schematic synthesis process for the MAPbBr$_3$@PbBr(OH) is illustrated in Fig. 1. The pH value of *N,N*-dimethylformamide (DMF) was preadjusted to 9.0 through dropwise addition of ammonium hydroxide; a mixture of PbBr$_2$ and MABr with a mole ratio of 1.05:1 was dissolved in DMF solvent under continuous stirring until a white precipitate was formed. Subsequently, the precipitate was placed into an oven at 70 °C to obtain dried MAPbBr$_3$ perovskite, as shown in the middle of Fig. 1. The dried MAPbBr$_3$ perovskite is named MA-d for convenience, and the yellow MA-d exhibits very weak fluorescence under UV illumination. After addition of water, bright green fluorescence appears. Detailed characterizations indicate that MA-d changes to rod-shaped PbBr(OH), and MAPbBr$_3$ QDs are embedded in situ into the PbBr(OH) microrods to form MAPbBr$_3$@PbBr(OH). MAPbBr$_3$@PbBr(OH) is named MA-h for convenience. Based on the first-principles calculations, the bandgap of PbBr(OH) is ~3.1 eV, which is close to the bandgap of the material (3.44 eV). The valence band maximum originates
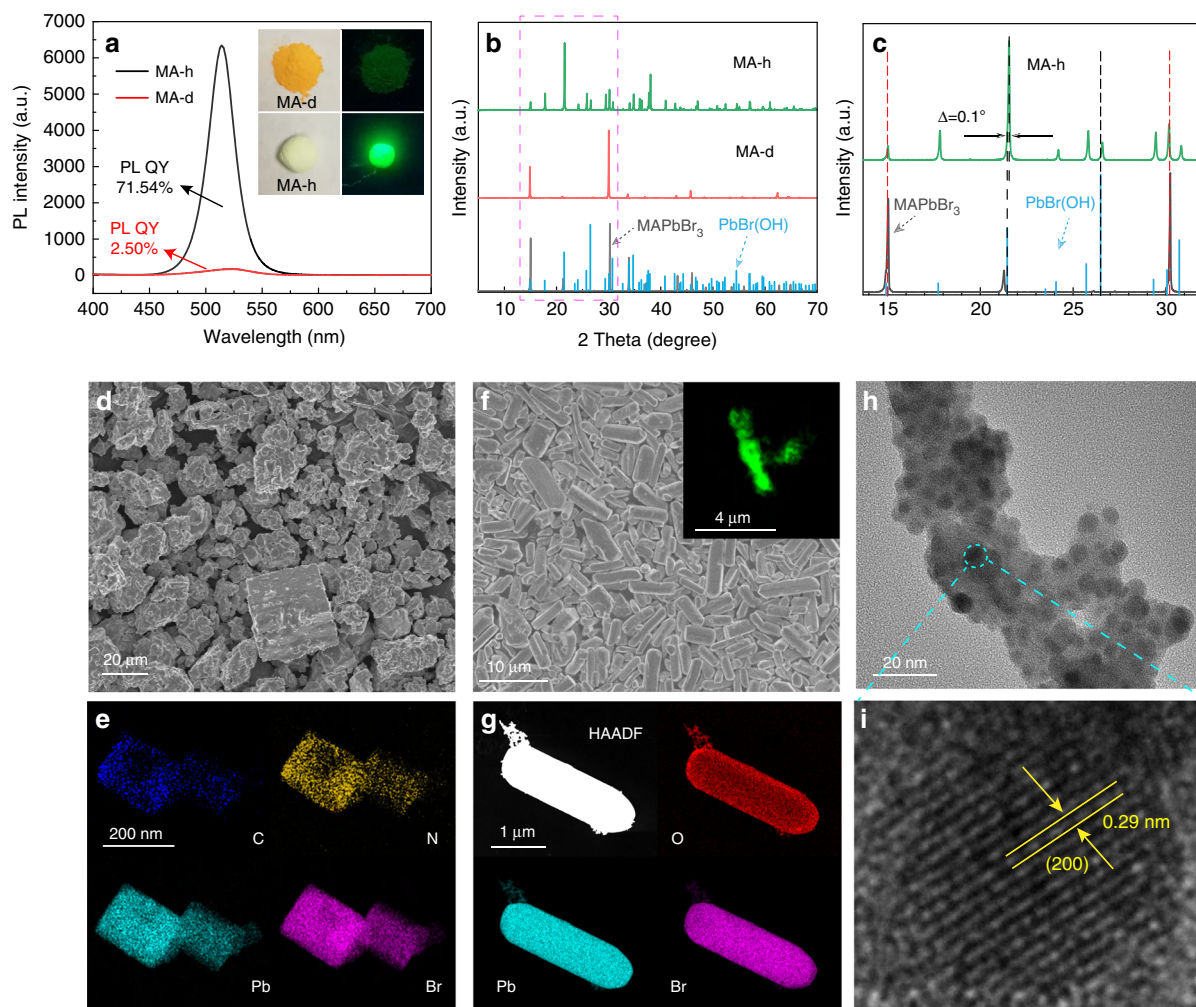
Fig. 2 a PL spectra of MA-d (PL QY: 2.50%) and MA-h (PL QY: 71.54%), and the inset shows the corresponding optical images of the two samples under indoor lighting and UV illumination. **b** XRD patterns of MA-d and MA-h. **c** Magnification of regions marked in **b**. **d** SEM image of MA-d. **e** Elemental mapping of MA-d. **f** SEM image of MA-h, and the inset shows a laser confocal fluorescence microscopy image. **g** Elemental mapping of MA-h. **h** TEM image of the crushed MA-h. **i** HRTEM image of the QDs in MA-h

from the Br and O orbitals, and the conduction band (CB) minimum is dominated by the Pb orbitals, as shown in Supplementary Fig. 1. The decomposition enthalpies of $MAPbBr_3$ and PbBr(OH) are 0.38 and 16.15 eV, respectively, (Supplementary Fig. 2, Supplementary Table 1), indicating that PbBr(OH) has higher thermodynamic stability than $MAPbBr_3$, which can prevent the decomposition of internal $MAPbBr_3$ QDs. Different from that apt to degrade and lose fluorescence in the presence of moisture[43], the MA-h synthesized in this work can maintain its bright fluorescence for a year in water.

The MA-d powders are yellow in color and show negligible green fluorescence under UV illumination. The MA-h powders are a greenish color and show bright green fluorescence under UV illumination, and the corresponding picture is shown in the inset of Fig. 2a. The fluorescence spectra of MA-d and MA-h are shown in Fig. 2a, and the emission intensity of MA-h increases 35-fold compared with that of MA-d. To compare the PL peaks of MA-d and MA-h, their PL intensities were normalized, as shown in Supplementary Fig. 3. The PL peak of MA-d is located at 523 nm, while that of MA-h is located at 514 nm, indicating that the size of MA-d decreases after adding water. In addition, the full-width at half-maximum (FWHM) of MA-d is 51 nm, and the FWHM of MA-h is only 26 nm, indicating the smaller and uniform size distribution of MA-h. The crystal structures of MA-d and MA-h were characterized by X-ray diffraction (XRD), as shown in Fig. 2b. All the diffraction peaks of MA-d are from the cubic perovskite structure of

$MAPbBr_3$, while the spectrum of MA-h contains many extra peaks in addition to those of $MAPbBr_3$, and the extra peaks can be assigned to PbBr(OH) (JCPDS No. 89–2492), indicating the formation of PbBr(OH). The enlarged XRD pattern (Fig. 2c) reveals that the diffraction peaks slightly shift to higher angles by ~0.1° compared with the standard data of PbBr(OH), which might be a result of the lattice mismatch between PbBr(OH) and $MAPbBr_3$. To further investigate the structural evolution of the samples before and after adding water, scanning electron microscopy (SEM) images and transmission electron microscopy (TEM) images were taken. Before adding water, MA-d is a typical cubic structure (Fig. 2d), which matches well with its XRD results. To further explore the microscopic morphology of the samples, the MA-d powders were broken by an ultrasonic cell crusher in toluene. In the TEM image of the crushed MA-d (Supplementary Fig. 4), monodisperse and uniform QDs (10 nm in size) with cubic shapes can be observed, and the QDs tend to agglomerate on the TEM grids, as previously reported[44]. The inset of Supplementary Fig. 4 highlights that MA-d possesses a well-defined crystalline structure with a characteristic lattice distance of 0.58 nm, corresponding to the d-spacing of the (100) crystal planes of $MAPbBr_3$. C, N, Pb, and Br can be observed from the elemental mapping of MA-d (Fig. 2e); the elements of C and N come from methylamine, while the elements of Pb and Br stem from the $PbBr_6$ octahedron. MA-h exhibits uniform rod morphology with an average diameter of 1.5 μm and length of 4 μm, as shown in Fig. 2f and Supplementary Fig. 5. The inset of Fig. 2f shows the corresponding laser confocal fluorescence microscope image, and uniform green fluorescence can be observed along the rod structure. Elemental mapping of MA-h is shown in Fig. 2g, and the elements O, Pb, and Br are uniformly distributed along the rod structure, which indicates the formation of PbBr(OH). To explore the inner structure of the rod, the MA-h powders were broken in a cell crusher. Some spherical QDs with an outer shell can be observed (Fig. 2h), and the lattice spacing of the QDs is 0.29 nm, corresponding to the d-spacing of the (200) crystal planes of $MAPbBr_3$ (Fig. 2i). The above results confirm that the $MAPbBr_3$ QDs were coated by PbBr(OH). Thus, one can conclude that the bulk cubic shape of $MAPbBr_3$ changes to a rod-like shape through the addition of water, and the $MAPbBr_3$ QDs are embedded into PbBr(OH). In addition, X-ray photoelectron spectroscopy (XPS) spectra were collected to detect the surface chemistry of MA-d and MA-h, as shown in Supplementary Fig. 6. The Br/Pb atomic ratios calculated from the XPS spectra are summarized in Supplementary Table 2. From the table, one can see that the Br/Pb atomic ratios of MA-d and MA-h are 3.06 and 1.11, respectively, confirming that these materials are $MAPbBr_3$ and PbBr(OH).

Discussion

Photophysical property

To evaluate the stability of the as-prepared perovskites, a repetitive hydrate–dehydrate cycle test was carried out, and the change in the PL intensity was monitored, as shown in Fig. 3a. The PL intensity of the MA-d perovskite increases instantly with the addition of water, accompanied by a color change from yellow to greenish. The perovskite gradually turns back to a yellow color after drying at 60 °C. As the hydrating–dehydrating cycle repeats, the PL intensity of MA-h decreases, while the color of the sample gradually stabilizes at greenish under ambient conditions. Additionally, the PL intensity of MA-d increases after several hydrating–dehydrating cycles, with its yellow color changing to a greenish color. The corresponding evolution of the PL spectra and the color of both samples are shown in Supplementary Figs. 7 and 8. In the first round, the PL QY of MA-d is only 2.5% and increases to 71.54% after the addition of water. The sample is held in water for 1 year, and the PL QY of the MA-h is still at 89.9% of its initial value, i.e., 64.28%, which is one of the most stable fluorescence perovskite powders ever reported to the best of our knowledge. A slight hypsochromic shift of PL is observed during the hydrating–dehydrating cycles, as evidenced by the normalized PL spectra shown in Fig. 3b. The continuous hypsochromic shift in the PL spectra might be a consequence of the decrease in the perovskite QD size during cycling. In addition, traditional LHPs are highly sensitive to polar solvents due to their inherent ionic crystal structure, and the optical properties and even structural integrity of these materials usually deteriorate in polar organic solvents[30]. However, in our work, the MA-h powders show ultrastability to many common organic solvents, such as DMSO, dimethyl formamide, ethanol, acetone, ethylacetate, and benzene. The PL spectra of the MA-h powders immersed in these organic solvents are shown in Fig. 3c, d, and the corresponding images under UV illumination are shown in the insets of Fig. 3c, d. The emission of the MA-h powders is stable in the different organic solvents, and no obvious emission peak shift is observed. In Supplementary Fig. 9, no obvious structural or morphological changes are observed in DMF or DMSO, indicating that PbBr(OH) is almost insoluble in common solvents, which is why MA-h can maintain good stability. Thermal stability is another important indicator for luminescent materials[45], especially for LHPs. Thermo-induced particle regrowth would induce PL quenching, and the crystal structure of the perovskites would collapse directly under exceedingly high temperatures. Additionally, high temperature might accelerate the rates of oxidation and hydration, which means that the oxygen- and moisture-induced decomposition would be amplified, leading to more rapid PL quenching[30]. Fig. 3e shows the

Fig. 3 a The PL intensity of the sample during cycling. **b** The corresponding PL spectra of MA-h, and the inset is the magnified spectra. **c, d** The PL spectra and images of the MA-h powders immersed in different solvents. **e** The PL intensity of the sample in the presence of water at different temperatures, and the inset is the schematic diagram of the reaction. **f** The PL intensity of the sample in the presence of water under UV irradiation for different hours, and the inset shows the schematic diagram of the test
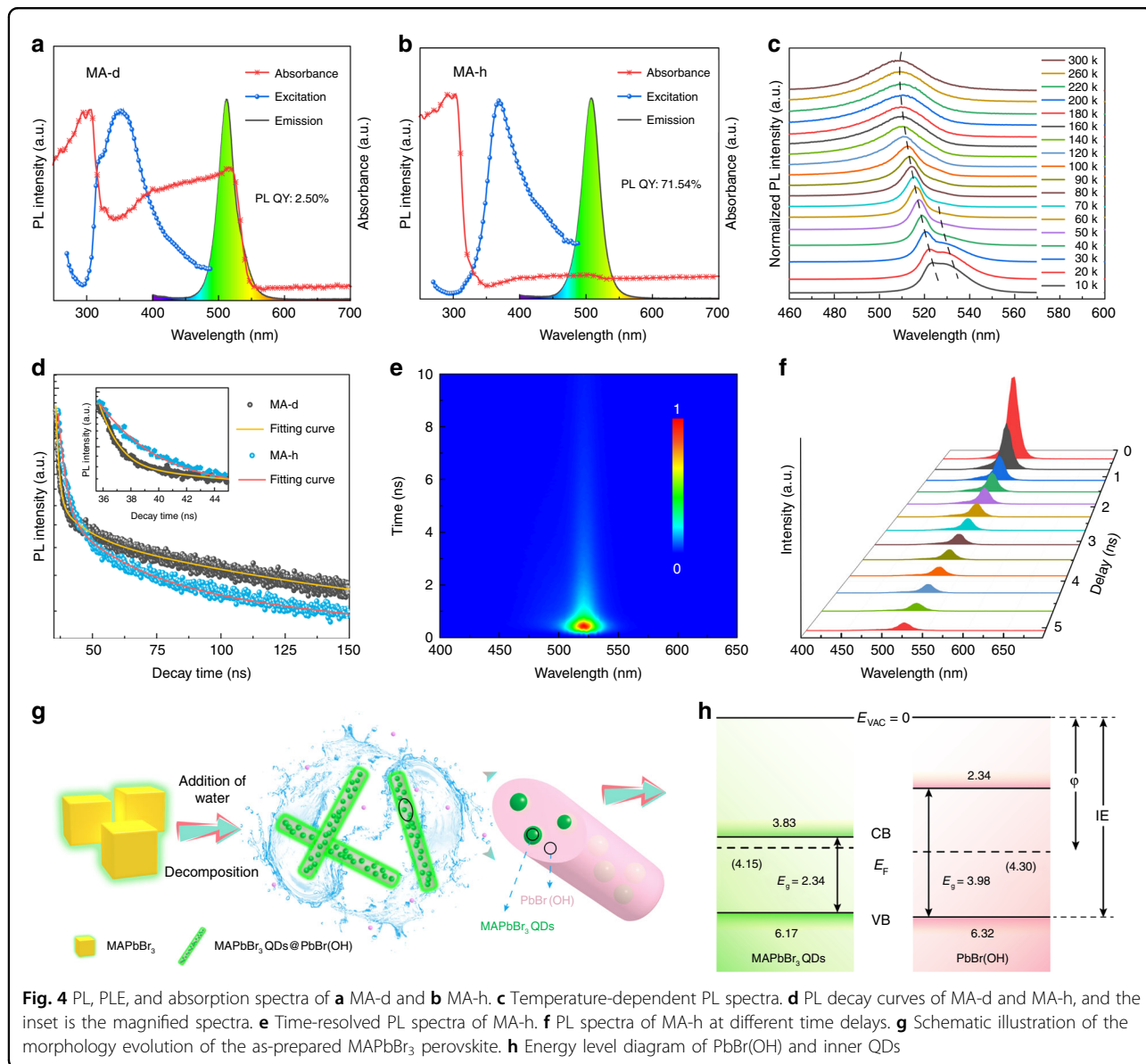
thermal stability of MA-h in the temperature range from 20 °C to 180 °C, and the corresponding PL spectra are shown in Supplementary Fig. 10. It is worth noting that the entire test process was carried out in an autoclave filled with water. It can be clearly seen that the PL intensity of MA-h decreases slowly as the temperature increases in the range of 20–100 °C, indicating good thermal stability. Upon heating above 100 °C, the PL intensity decreases sharply and eventually vanishes when the temperature reaches 180 °C. The PL decrease is due to the destruction of dense matrix PbBr(OH), and the corresponding XRD and SEM images are shown in Supplementary Fig. 11. In addition, the PL intensity of MA-h is still at 78.7% of the initial intensity upon heating from 20 °C to 100 °C. The photostability of MA-h was also investigated. Figure 3f shows the PL spectra of MA-h under continuous irradiation with a UV lamp (365 nm, 0.15 mW/cm^2), and the corresponding PL spectra are shown in Supplementary Fig. 12. The intensity decreases sharply during the first 24 h and maintains 50% of the initial intensity after 60 h of UV illumination. Supplementary Fig. 13 shows the XRD patterns and SEM images of MA-h under UV irradiation, and no obvious structural or morphological changes can be observed. According to previous studies, a possible reason for the PL decrease under UV illumination is photoassisted ionization or

photoinduced defects[46,47]. The above results indicate that MA-h has good ambient, thermal, and photostability.
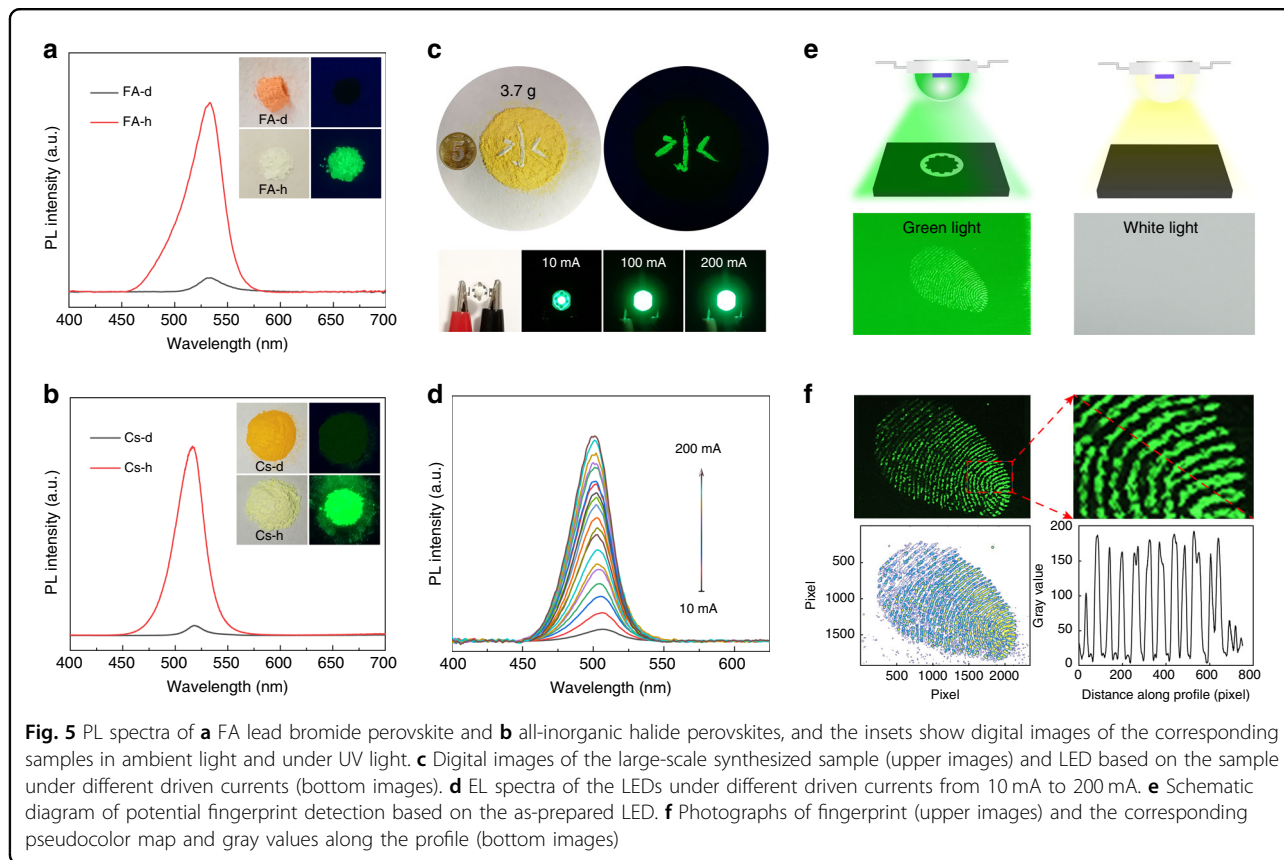
Mechanism for enhanced efficiency

To further investigate the high PL QY and the luminescence mechanisms of the as-prepared perovskite in the presence of water, the steady-state PL spectra, absorption spectra, time-resolved spectra, and temperature-dependent PL spectra of the as-prepared perovskite were recorded, as shown in Fig. 4. The PL, PL excitation (PLE), and absorption spectra of the as-prepared MA-d perovskite are shown in Fig. 4a, and the samples have strong absorption at 516 nm. Figure 4b shows the PL, PLE, and absorption spectra of MA-h, from which semblable PL and excitation characteristics can be observed, while obvious differences are observed in the absorption spectra. Compared with MA-h, MA-d has a significant absorption peak at 516 nm that absorbs the emissions of MA-d. The absorption peak centered at ~310 nm with an absorption edge of 360 nm can be ascribed to the absorption of PbBr(OH). To further understand the luminescence mechanism of MA-h, temperature-dependent PL measurements were carried out with temperatures from 10 K to 300 K. In Fig. 4c, the PL peak (523 nm) at 10 K is as narrow as 6.8 nm, which originates from the emission of a typical strong excitonic

Fig. 4 PL, PLE, and absorption spectra of **a** MA-d and **b** MA-h. **c** Temperature-dependent PL spectra. **d** PL decay curves of MA-d and MA-h, and the inset is the magnified spectra. **e** Time-resolved PL spectra of MA-h. **f** PL spectra of MA-h at different time delays. **g** Schematic illustration of the morphology evolution of the as-prepared MAPbBr$_3$ perovskite. **h** Energy level diagram of PbBr(OH) and inner QDs

recombination[31]. With the increasing temperature, the intensity of the peak centered at 530 nm (at 10 K) gradually decreases and ultimately disappears at 60 K. Additionally, a new emission peak appears in the shorter wavelength range that corresponds to free exciton emissions. By tracking the PL evolution versus temperature, we clearly reveal that the PL of MA-h at room temperature is dominated by free exciton emissions. The lifetimes of the as-prepared perovskites with and without water were recorded, as shown in Fig. 4d. Both PL decay curves of MA-d and MA-h can be fitted well by a three-exponent function, and the concrete values are summarized in Supplementary Table 3. The average lifetime of MA-h is 2.50 ns, which is longer than that of MA-d (1.08 ns). This result is supported by the time-resolved spectrum of MA-h, as shown in Fig. 4e. The longer PL lifetime and higher PL intensity of MA-h indicate a lower trap-state density[48], which suggests that PbBr(OH) effectively passivates the defect sites in MAPbBr$_3$ perovskite. In addition, oxygen molecules can increase the PL efficiency in bulk structures but have the opposite effect in QDs[49]. The instability of halide perovskite caused by ion migration is a possible issue[50]. Ion migrations are usually caused by halide vacancies, and the halide vacancies are passivated by the Br ions of PbBr(OH) in this work. Therefore, this strategy can decrease the instability caused by ion migration. Figure 4f shows the 3D plot of the PL spectra at various times, revealing an essentially time-independent spectral shape of PL emissions. In addition, the FWHM and emission peak are recorded in Supplementary Fig. 14, and the results suggest an absence of peak shifting or broadening.

Fig. 5 PL spectra of **a** FA lead bromide perovskite and **b** all-inorganic halide perovskites, and the insets show digital images of the corresponding samples in ambient light and under UV light. **c** Digital images of the large-scale synthesized sample (upper images) and LED based on the sample under different driven currents (bottom images). **d** EL spectra of the LEDs under different driven currents from 10 mA to 200 mA. **e** Schematic diagram of potential fingerprint detection based on the as-prepared LED. **f** Photographs of fingerprint (upper images) and the corresponding pseudocolor map and gray values along the profile (bottom images)

To further investigate the formation mechanism of MA-h in the presence of water, we studied the morphological evolution of MA-h, and a possible mechanism was proposed. The morphological evolution of MA-h during the drying process was observed by optical microscopy and fluorescence microscopy. In Supplementary Fig. 15, the MA-h self-assembles into a cubic structure with loss of water, and then the rod structure forms again after water is added. Figure 4g shows a schematic illustration of the formation process of the as-prepared sample in the presence of water. Initially, yellow bulk perovskite with NH^{4+} and OH^- attached to the surface is produced. With the addition of water, the yellow bulk perovskite is destroyed and decomposes from the outside to inside, and $PbBr(OH)$ is simultaneously formed with the aid of OH^- during this process. A portion of the decomposed small crystals (QDs) are wrapped into rod-shaped $PbBr(OH)$ by oriented self-assembly. The sample exhibits improved PL QY and ultrahigh stability due to the formation of $MAPbBr_3$ QDs embedded into the $PbBr(OH)$ matrix. With the volatilization of water during the drying process, $PbBr(OH)$ reacts with precipitated MABr (MABr is soluble in water) to form cubic perovskite. Correspondingly, the color of the sample changes from greenish to yellow, and the fluorescence intensity decreases after drying. Subsequently, each cycle (adding water and

drying) produces a similar phenomenon until all the MABr is taken away by water and the perovskite QDs are entirely coated by $PbBr(OH)$. Therefore, the color of the sample gradually changes to greenish in ambient light, and ultrastable $MAPbBr_3@PbBr(OH)$ is formed. The energy level of the $MAPbBr_3$ QDs and $PbBr(OH)$ was studied by ultraviolet photoelectron spectroscopy (UPS), which can provide both the ionization potential and the valence band (VB) level of the sample, as well as its work function (ϕ). By combining UPS (Supplementary Fig. 16) and absorption spectra, we can establish the energy level. In Fig. 4h, the CB of the matrix ($PbBr(OH)$) is higher than that of the QDs, while the VB of the matrix is lower than that of the QDs. As a result, the surface defects are passivated by $PbBr(OH)$, and both electrons and holes are confined in the QDs. The band alignment between the inner QDs and the outer matrix can guarantee exciton generation and high-rate radiative recombination of the QDs, thus resulting in a sharp PL QY.

Application to LEDs

Interestingly, this strategy is universal to other bromide perovskites, including $FAPbBr_3$ perovskites and $CsPbBr_3$. The PL spectra of $FAPbBr_3$ are shown in Fig. 5a. The corresponding optical properties, structure, and morphology are shown in Supplementary Figs. 17 and 18.

Table 1 Summary of PL properties and stability of perovskite QDs

Strategy	Perovskite	Emission peak (nm)	FWHM (nm)	PL QYs (%)	Stability	Ref.
Compositional engineering	$CsPbBr_3$ QDs	513	20	95	90% (30 d, air)	[31]
	$FAPbBr_3$ NCs	530	22	85	38% (100 °C)	[51]
	$CsPbBr_3$: Mn QDs	514–517	20	90	60% (120 d, air)	[52]
Surface engineering	$MAPbBr_3$–APTES NCs	505	42	55	70% (2.5 h, isopropanol)	[53]
	$CsPbBr_3$–TDPA QDs	522	22	68	80% (300 min, water)	[54]
	$CsPbBr_3$–CTAB QDs	515	39	71	63% (80 min, UV)	[55]
Matrix encapsulation	$CsPbBr_3$–Meso-SiO_2 QDs	515	20	55	60% (100 °C)	[33]
	$CsPbBr_3$–Ami-SiO_2 powders	520	26	56	80% (108 h, UV)	[47]
	$CsPbBr_3$–PMMA powders	510	25	45	75% (3 d, air)	[56]
	$MAPbBr_3$ powders	518	50	11.7	82% (6 months, water)	[42]
	$CsPbBr_3$ powders	508	45	53.9	74% (6 months, water)	[42]
	$MAPbBr_3$ powders	514	28	71.5	90% (1 year, water, DMF), 80% (100 °C, water), 50% (60 h, UV)	Our work

Figure 5b shows the PL spectra of $CsPbBr_3$, and the corresponding optical properties, structure, and morphology are shown in Supplementary Figs. 19 and 20. In addition, $MAPb(Br/I)_3@Pb(Br/I)(OH)$ was prepared by this method, and the corresponding spectrum and image are shown in Supplementary Fig. 21. The fluorescence peak redshifts to ~630 nm, indicating that the emissions can be tuned by changing the X site anion. Notably, this method is simple and facile, and the samples can be prepared on a large scale by proportionally enlarging the precursors, as shown in Fig. 5c. Three grams of the powders are obtained in one synthesis process, and no obvious differences are observed from batch to batch. A Chinese character was written in the samples using water as ink; the regions with water are greenish in color and show bright green fluorescence under UV illumination. As discussed above, compared to traditional perovskites, synthetic powders have improved ambient, thermal, and photostabilities, and the reported perovskites with improved stability are summarized in Table 1. High PL QY and stability can be achieved simultaneously for the first time in this work. Based on these merits, this material can be employed as a promising phosphor in LEDs. UV-pumped LEDs were fabricated by coating the MA-h and PDMS mixture onto 365 nm UV chips. Bright green light with color coordinates of (0.21, 0.52) can be observed (Supplementary Fig. 22), and the emission intensity of the LEDs increases as the drive current increases (Supplementary Fig. 23). The light output of the LED versus time was measured, as shown in Supplementary Fig. 24. The initial luminous intensity of the LED is 1061 cd/m^2, and the intensity decreases with running time. The luminous intensity of the LED settles at ~400 cd/m^2 after 480 min (8 h) of running. The luminescence intensity of the as-prepared LEDs can reach 9549 cd/m^2 when the driving current increases to 200 mA. The corresponding EL spectra of the LEDs under different drive currents from 10 mA to 200 mA are shown in Fig. 5d. In addition, an LED with bright green light can improve the contrast of illuminated objects due to the sensitivity of human eyes to green light. Thus, the as-prepared LEDs are suitable for manual defect detection. As illustrated in Fig. 5e, the light of the LED shines on the surface of the object; thus, the blemishes on the surface of the object (such as scratches, dust, and fingerprints) can be clearly observed. The different defects on the surface of substrates under illumination with a white LED and the as-prepared LED are shown in Supplementary Figs. 25 and 26. Under irradiation with green light, the fingerprint on the glass is extracted (Fig. 5f), and the fingerprint can be observed clearly. The corresponding pseudocolour map and gray values along the lines in Fig. 5f (bottom images) further indicates the resolution of the image.

In summary, we synthesized bromide-based perovskites whose PL QY can be increased from 2.5% to 71.54% by introducing water and decreases minimally in aqueous solution in 1 year. In addition, the as-synthesized $MAPbBr_3@PbBr(OH)$ can maintain their luminescence in many kinds of solvents and also exhibit excellent ambient, thermal, and photostabilities. The enhanced

stability and PL QY can be attributed to the water-induced $MAPbBr_3@PbBr(OH)$. $PbBr(OH)$ passivated the defects of the $MAPbBr_3$ QDs and confined carriers within the QDs so that $MAPbBr_3@PbBr(OH)$ could reach high emission efficiency; additionally, $PbBr(OH)$ can prevent the exposure of the QDs to air and moisture, thus increasing the stability. This strategy is universal to $MAPbBr_3$, $FAPbBr_3$, and $CsPbBr_3$. UV chip-pumped LEDs were fabricated by using the sample as promising phosphors, and the luminance intensity of the device was as high as $9549 \, cd/m^2$. Furthermore, blemishes including scratches, dust, and fingerprints on the surface of glass could be observed under the illumination of the LEDs, indicating that they are suitable for manual defect detection. This efficient approach for the synthesis of ultrastable and highly efficient luminescent perovskites will push forward their practical applications.

Materials and methods

The materials used were methylamine (CH_3NH_2; 32% wt/wt aq. soln), hydrobromic acid (HBr, 48% wt/wt aq. soln), lead bromide ($PbBr_2$; >98%, Aladdin), ammonium hydroxide ($NH_3 \cdot H_2O$; 27% wt/wt aq. soln), and DMF (>99.8%, Aladdin). All the reagents were used directly without further purification.

Synthesis of methylammonium bromide

Methylammonium bromide (CH_3NH_3Br) was prepared by slowly mixing methylamine with HBr at a 1:1 molar ratio under continuous stirring for 2 h at 0 °C. CH_3NH_3Br was then crystallized by removing the solvent from an evaporator. Then, the CH_3NH_3Br was washed with diethyl ether three times. White powders were obtained by recrystallization with ethanol. Subsequently, the powders were dried in vacuum for 24 h and stored in a dark and dry environment for further use.

Synthesis of $MAPbBr_3$ perovskites

The pH of DMF was preadjusted with ammonium hydroxide, and the pH was ~9. Then, 2.31 g $PbBr_2$ and 0.67 g MABr (the molar ratio of $PbBr_2$ to MABr was 1.05) were dissolved in 6 ml alkaline DMF mixed solution to form a white viscous solution, and then the solution was continuously stirred until a white-colored precipitate was formed. Subsequently, the precipitate was centrifuged at 7500 rpm, and the precipitate was placed into an oven at 70 °C to obtain $MAPbBr_3$ perovskite powders. $MAPbBr_3$ can be converted to bright emissive $MAPbBr_3@PbBr(OH)$ through the addition of water.

Synthesis of $MAPbBr_3@PbBr(OH)$

The synthesis details of $MAPbBr_3@PbBr(OH)$ are as follows: 1 g of the as-prepared $MAPbBr_3$ powder was added to 10 ml of water, and then the mixture was stirred for 1 min. The process was replicated several times until the yellow MAPbBr3 powder transformed into greenish $MAPbBr_3@PbBr(OH)$ powder.

Synthesis of $MAPb(Br/I)_3@Pb(Br/I)(OH)$

One gram of the as-prepared $MAPbBr_3@PbBr(OH)$ was homogeneously mixed with KI at a mass ratio of 1:2, and then $MAPb(Br/I)_3@Pb(Br/I)(OH)$ was obtained after several minutes.

Fabrication of LEDs

First, the as-prepared MA-h phosphors were uniformly mixed with PDMS. The mixture of MA-h and PDMS was debubbled, and coated onto a 365 nm UV chip and then cured in an oven at 70 °C for 1 h to obtain UV-pumped LEDs.

Characterization

The XRD patterns were obtained by an X'Pert Pro diffractometer. The TEM images were taken by a transmission electron microscope (JEM-2010), and the SEM images were obtained on a JEOL JSM6700F field-emission scanning electron microscope. The Fourier transform infrared (FTIR) spectra of the samples were recorded on a Thermo Scientific Nicolet iS10 FTIR spectrometer. The PL QYs of the samples were measured by an Edinburgh fluorescence spectrometer (FLS980). The X-ray photoelectron spectra of the samples were collected by a Thermo Fisher Scientific ESCALAB 250Xi spectrometer equipped with an Al Ka X-ray radiation source, and the XPS binding energy was internally referenced to the C 1 s peak (BE = 284.8 eV). The PL spectra were measured by a Hitachi F-7000 spectrophotometer, and the UV–vis absorption spectra were characterized by a UH4150 spectrophotometer.

Computational methods

All the first-principle calculations were performed utilizing the plane-wave pseudopotential approach within density functional theory as implemented in the Vienna Ab initio Simulation Package. The 1 s for H, $2s^2 2p^2$ for C, $2s^2 2p^3$ for N, $2s^2 2p^4$ for O, $6s^2 6p^2$ for Pb, and $4s^2 4p^5$ for Br were treated as valence electrons, and the interactions between nucleus and valence electrons were described by the projected augmented wave method. The electronic wave functions were expanded in plane-wave basis sets with a kinetic energy of 400 eV, and Brillouin zone sample meshes with $2\pi \times 0.02 \, Å^{-1}$ were utilized to ensure the energy convergence of our calculations.

Author contributions

K.-K.L. and Q.L. contributed equally to this work. K.-K.L. conceived the idea; C.-X. S., L.D., and K.-K.L. supervised and coordinated all aspects of this project. Q.L. carried out the synthesis and characterization, and Q.L. and K.-K.L. wrote the paper. Y.-C.L. fabricated the LEDs. L.-Z.S. measured the time-resolved spectra. D.-W.Y., J.-Y.W., W.-B.Z. and X.-Y.W. commented on the paper, and all of the authors discussed the results.

Data availability

The data that support the findings of this study are available from the corresponding authors upon reasonable request.

Conflict of interest

The authors declare that they have no conflict of interest.

References

1. Lee, M. M. et al. Efficient hybrid solar cells based on meso-superstructured organometal halide perovskites. *Science* **338**, 643–647 (2012).
2. Burschka, J. et al. Sequential deposition as a route to high-performance perovskite-sensitized solar cells. *Nature* **499**, 316–319 (2013).
3. Liu, M. Z., Johnston, M. B. & Snaith, H. J. Efficient planar heterojunction perovskite solar cells by vapour deposition. *Nature* **501**, 395–398 (2013).
4. Jeon, N. J. et al. Solvent engineering for high-performance inorganic-organic hybrid perovskite solar cells. *Nat. Mater.* **13**, 897–903 (2014).
5. Hoye, R. L. Z. et al. Enhanced performance in fluorene-free organometal halide perovskite light-emitting diodes using tunable, low electron affinity oxide electron injectors. *Adv. Mater.* **27**, 1414–1419 (2015).
6. Jeon, N. J. et al. Compositional engineering of perovskite materials for high-performance solar cells. *Nature* **517**, 476–480 (2015).
7. Zhu, H. M. et al. Lead halide perovskite nanowire lasers with low lasing thresholds and high quality factors. *Nat. Mater.* **14**, 636–642 (2015).
8. Senanayak, S. P. et al. Understanding charge transport in lead iodide perovskite thin-film field-effect transistors. *Sci. Adv.* **3**, e1601935 (2017).
9. Yang, W. S. et al. High-performance photovoltaic perovskite layers fabricated through intramolecular exchange. *Science* **348**, 1234–1237 (2015).
10. Chao, X. et al. Ultrasensitive broadband phototransistors based on perovskite/organic-semiconductor vertical heterojunctions. *Light.: Sci. Appl.* **6**, e17023 (2017).
11. Li, J. H. et al. 50-Fold EQE improvement up to 6.27% of solution-processed all-inorganic perovskite CsPbBr$_3$ QLEDs via surface ligand density control. *Adv. Mater.* **29**, 1603885 (2017).
12. Fang, H. H. et al. Photoexcitation dynamics in solution-processed formamidinium lead iodide perovskite thin films for solar cell applications. *Light. Sci. Appl.* **5**, e16056 (2016).
13. Zhang, T. Y. et al. Bication lead iodide 2D perovskite component to stabilize inorganic α-CsPbI$_3$ perovskite phase for high-efficiency solar cells. *Sci. Adv.* **3**, e1700841 (2017).
14. Zhao, Y. C. et al. Quantification of light-enhanced ionic transport in lead iodide perovskite thin films and its solar cell applications. *Light. Sci. Appl.* **6**, e16243 (2017).
15. Lin, J. et al. Thermochromic halide perovskite solar cells. *Nat. Mater.* **17**, 261–267 (2018).
16. Kim, Y. H. et al. Multicolored organic/inorganic hybrid perovskite light-emitting diodes. *Adv. Mater.* **27**, 1248–1254 (2015).
17. Shi, Z. F. et al. High-efficiency and air-stable perovskite quantum dots light-emitting diodes with an all-inorganic heterostructure. *Nano Lett.* **17**, 313–321 (2017).
18. Sun, H. Z. et al. Chemically addressable perovskite nanocrystals for light-emitting applications. *Adv. Mater.* **29**, 1701153 (2017).
19. Cao, Y. et al. Perovskite light-emitting diodes based on spontaneously formed submicrometre-scale structures. *Nature* **562**, 249–253 (2018).
20. Lin, K. B. et al. Perovskite light-emitting diodes with external quantum efficiency exceeding 20 per cent. *Nature* **562**, 245–248 (2018).
21. Ramasamy, P. et al. All-inorganic cesium lead halide perovskite nanocrystals for photodetector applications. *Chem. Commun.* **52**, 2067–2070 (2016).
22. Swarnkar, A. et al. Quantum dot-induced phase stabilization of α-CsPbI$_3$ perovskite for high-efficiency photovoltaics. *Science* **354**, 92–95 (2016).
23. Kovalenko, M. V., Protesescu, L. & Bodnarchuk, M. I. Properties and potential optoelectronic applications of lead halide perovskite nanocrystals. *Science* **358**, 745–750 (2017).
24. Wang, Y. et al. Solution-processed low threshold vertical cavity surface emitting lasers from all-inorganic perovskite nanocrystals. *Adv. Funct. Mater.* **27**, 1605088 (2017).
25. Wang, Y. et al. All-inorganic colloidal perovskite quantum dots: a new class of lasing materials with favorable characteristics. *Adv. Mater.* **27**, 7101–7108 (2015).
26. Sutton, R. J. et al. Bandgap-tunable cesium lead halide perovskites with high thermal stability for efficient solar cells. *Adv. Energy Mater.* **6**, 1502458 (2016).
27. Chen, W. W. et al. Enhanced stability and tunable photoluminescence in perovskite CsPbX$_3$/ZnS quantum dot heterostructure. *Small* **13**, 1604085 (2017).
28. Li, X. M. et al. All inorganic halide perovskites nanosystem: synthesis, structural features, optical properties and optoelectronic applications. *Small* **13**, 1603996 (2017).
29. Wu, C. et al. Improved performance and stability of all-inorganic perovskite light-emitting diodes by antisolvent vapor treatment. *Adv. Funct. Mater.* **27**, 1700338 (2017).
30. Wei, Y., Cheng, Z. Y. & Lin, J. An overview on enhancing the stability of lead halide perovskite quantum dots and their applications in phosphor-converted LEDs. *Chem. Soc. Rev.* **48**, 310–350 (2019).
31. Li, X. M. et al. CsPbX$_3$ quantum dots for lighting and displays: room-temperature synthesis, photoluminescence superiorities, underlying origins and white light-emitting diodes. *Adv. Funct. Mater.* **26**, 2435–2445 (2016).
32. Tan, Y. S. et al. Highly luminescent and stable perovskite nanocrystals with octylphosphonic acid as a ligand for efficient light-emitting diodes. *ACS Appl. Mater. Interfaces* **10**, 3784–3792 (2018).
33. Wang, H. C. et al. Mesoporous silica particles integrated with all-inorganic CsPbBr$_3$ perovskite quantum-dot nanocomposites (MP-PQDs) with high stability and wide color gamut used for backlight display. *Angew. Chem. Int. Ed.* **55**, 7924–7929 (2016).
34. Jia, C. et al. CsPbX$_3$/Cs$_4$PbX$_6$ core/shell perovskite nanocrystals. *Chem. Commun.* **54**, 6300–6303 (2018).
35. Tang, X. S. et al. CsPbBr$_3$/CdS core/shell structure quantum dots for inverted light-emitting diodes application. *Front. Chem.* **7**, 499 (2019).
36. Zhong, Q. X. et al. One-pot synthesis of highly stable CsPbBr$_3$@SiO$_2$ core-shell nanoparticles. *ACS Nano* **12**, 8579–8587 (2018).
37. Wang, B. et al. Postsynthesis phase transformation for CsPbBr$_3$/Rb$_4$PbBr$_6$ core/shell nanocrystals with exceptional photostability. *ACS Appl. Mater. Interfaces* **10**, 23303–23310 (2018).
38. Shoyama, K. et al. Effects of water on the forward and backward conversions of lead(ii) iodide to methylammonium lead perovskite. *J. Mater. Chem. A* **5**, 23815–23821 (2017).
39. Wu, L. Z. et al. From nonluminescent Cs$_4$PbX$_6$ (X = Cl, Br, I) nanocrystals to highly luminescent CsPbX$_3$ nanocrystals: water-triggered transformation through a CsX-stripping mechanism. *Nano Lett.* **17**, 5799–5804 (2017).
40. Turedi, B. et al. Water-induced dimensionality reduction in metal-halide perovskites. *J. Phys. Chem. C* **122**, 14128–14134 (2018).
41. Zhang, X. Y. et al. Water-assisted size and shape control of CsPbBr$_3$ perovskite nanocrystals. *Angew. Chem. Int. Ed.* **57**, 3337–3342 (2018).
42. Jana, A. & Kim, K. S. Water-stable, fluorescent organic−inorganic hybrid and fully inorganic perovskites. *ACS Energy Lett.* **3**, 2120–2126 (2018).
43. Huang, H. et al. Lead halide perovskite nanocrystals in the research spotlight: stability and defect tolerance. *ACS Energy Lett.* **2**, 2071–2083 (2017).
44. Chen, L. C. et al. An ultrasonic synthesis method for high-luminance perovskite quantum dots. *Ceram. Int.* **43**, 16032–16035 (2017).
45. Liang, Y. C. et al. Multi-zinc oxide-cores@uni-barium sulfate-shell with improved photo-, thermal-, and ambient-stability: non-equilibrium sorption fabrication and light-emitting diodes application. *J. Colloid Interface Sci.* **529**, 1–10 (2018).

46. Park, Y. S. et al. Room temperature single-photon emission from individual perovskite quantum dots. *ACS Nano* **9**, 10386–10393 (2015).

47. Li, X. M. et al. Amino-mediated anchoring perovskite quantum dots for stable and low-threshold random lasing. *Adv. Mater.* **29**, 1701185 (2017).

48. Lee, S. et al. Amine-based passivating materials for enhanced optical properties and performance of organic-inorganic perovskites in light-emitting diodes. *J. Phys. Chem. Lett.* **8**, 1784–1792 (2017).

49. Wang, Y. et al. Switching excitonic recombination and carrier trapping in cesium lead halide perovskites by air. *Commun. Phys.* **1**, 96 (2018).

50. Yang, D. W. et al. Fast diffusion of native defects and impurities in perovskite solar cell material $CH_3NH_3PbI_3$. *Chem. Mater.* **28**, 4349–4357 (2016).

51. Minh, D. N. et al. Room-temperature synthesis of widely tunable formamidinium lead halide perovskite nanocrystals. *Chem. Mater.* **29**, 5713–5719 (2017).

52. Zou, S. H. et al. Stabilizing cesium lead halide perovskite lattice through Mn(II) substitution for air-stable light-emitting diodes. *J. Am. Chem. Soc.* **139**, 11443–11450 (2017).

53. Luo, B. B. et al. Organolead halide perovskite nanocrystals: branched capping ligands control crystal size and stability. *Angew. Chem. Int. Ed.* **55**, 8864–8868 (2016).

54. Xuan, T. T. et al. Highly stable $CsPbBr_3$ quantum dots coated with alkyl phosphate for white light-emitting diodes. *Nanoscale* **9**, 15286–15290 (2017).

55. Cai, Y. T. et al. Improved stability of $CsPbBr_3$ perovskite quantum dots achieved by suppressing interligand proton transfer and applying a polystyrene coating. *Nanoscale* **10**, 21441–21450 (2018).

56. Ma, K. Z. et al. *In situ* fabrication of halide perovskite nanocrystals embedded in polymer composites *via* microfluidic spinning microreactors. *J. Mater. Chem. C* **5**, 9398–9404 (2017).